NUMERICAL PREDICTION OF PERMEABILITY USING A LATTICE BOLTZMANN METHOD AND OPTICAL COHERENCE TOMOGRAPHY

Frederick R. Phelan Jr., Joy P. Dunkers, Carl G. Zimba,
Kathleen M. Flynn, Richard S. Parnas and Richard C. Peterson
Polymers Division
National Institute of Standards and Technology
Gaithersburg, MD 20899

Xingde Li and James G. Fujimoto
Department of Electrical Engineering
Massachusetts Institute of Technology
Cambridge, MA 02139

ABSTRACT

A rapid, non-destructive technique called optical coherence tomography (OCT) is used to image the microstructure of an epoxy/e-glass composite. The raw OCT data is processed and converted to a binary image, and then input into a lattice Boltzmann simulation for permeability prediction. Calculated permeabilities fall within the experimentally determined range for the same fiber volume fraction. The effect of different image processing algorithms which convert the raw grayscale OCT image to a binary image is discussed.

INTRODUCTION

Fluid flow in Liquid Composite Molding (LCM) processes such as resin transfer molding (RTM) is usually modeled using Darcy's Law given by

$$\boldsymbol{v} = -\frac{\boldsymbol{K}}{\mu} \cdot \nabla P \qquad \textbf{(1)}$$

where $\boldsymbol{v}$ is the average (superficial) velocity in the medium, P is the pressure, $\boldsymbol{K}$ is a symmetric, second order tensor known as the permeability and μ is the fluid viscosity. Determining the permeability tensor of preform materials in liquid composite molding applications is essential for process modeling and optimization calculations. Experimental determination of the permeability (1,2) yields accurate values for preforms laid out in flat sections, but such measurements are difficult and time consuming, and often do not apply to the deformed configurations the preform encounters when placed in a tool. Computational prediction of permeability (3-6) offers a potentially accurate and robust alternative to experimental methods. Such calculations involve imposing a pressure drop across the media, solving the appropriate transport equations for the detailed flow field, and then backcalculating the permeability by applying Darcy's law. The biggest drawback of this approach has been the inability to accurately determine the detailed geometry of the fibrous preform materials, which in addition to many intricate structural features, typically contain statistical variations and defects in their microstructure (7). Without a precise representation of the media, it is not possible to accurately predict permeability values using computational methods.

Optical coherence tomography (OCT) is a non-invasive, non-contact optical imaging technique that allows the visualization of microstructure within scattering media (8-10). OCT uses light in a manner analogous to the way ultrasound imaging uses sound, providing significantly higher spatial resolution (5-20 μm) albeit with shallower penetration depth. In this work, OCT was used to image an epoxy/unidirectional E-glass composite. The volumetric images were converted to binary using a number of different image processing routines and input into a flow simulation for prediction of axial and transverse permeabilities. The permeabilities predicted using the different routines are compared with experimental values.

NUMERICAL SIMULATION

Modeling of microscale flow in fibrous porous media is complicated by the existence of an open region around the tows, and a porous media inside the tows. Following previous studies (3-7), the Stokes equation, given by

$$\mu \nabla^2 \boldsymbol{v} = \nabla P \quad \textbf{(2)}$$

is used to model flow in the open regions, and the Brinkman equation, given by

$$\mu \nabla^2 \boldsymbol{v} - \mu \boldsymbol{K}_{tow}^{-1} \cdot \boldsymbol{v} = \nabla P \quad \textbf{(3)}$$

is used to model flow in the porous regions, where $\boldsymbol{K}_{tow}$ is the permeability of the porous tows. In both regions, the continuity equation

$$\nabla \cdot \boldsymbol{v} = 0 \quad \textbf{(4)}$$

is used to model conservation of mass.

Solutions to the governing equations above are obtained using a lattice Boltzmann method previously described in detail elsewhere (5,6). The method involves the solution of the discrete Boltzmann equation for the particle velocity distribution function $n_\alpha(\boldsymbol{x},t)$, where traditional fluid flow quantities such as density and velocity are obtained through the moment sums

$$\rho(\boldsymbol{x},t) = m \sum_{\alpha=1}^{N} n_\alpha(\boldsymbol{x},t) \tag{5}$$

$$\boldsymbol{u}(\boldsymbol{x},t) = \frac{m}{\rho(\boldsymbol{x},t)} \sum_{\alpha=1}^{N} \boldsymbol{v}_\alpha\, n_\alpha(\boldsymbol{x},t) \tag{6}$$

where $\rho(\boldsymbol{x},t)$ and $u(\boldsymbol{x},t)$ are the macroscopic fluid density and velocity, m is the mass of fluid, $\boldsymbol{v}_\alpha$ are components of the discrete velocity space, and N is the number of velocities comprising the velocity space. The particle distribution function $n_\alpha(\boldsymbol{x},t)$ is governed by the discrete Boltzmann equation given by

$$n_\alpha(\boldsymbol{x}+\boldsymbol{v}_\alpha,t+1) = n_\alpha(\boldsymbol{x},t) + \delta_\alpha(\boldsymbol{x},t) \tag{7}$$

where $\delta_\alpha(\boldsymbol{x},t)$ is the collision operator which couples the set of velocity states $\boldsymbol{v}_\alpha$. Most LB formulations employ the linear "BGK" form (5,6,12) of the collision operator in which the distribution function is expanded about its equilibrium value

$$\delta_\alpha = -\frac{n_\alpha(\boldsymbol{x},t) - n_\alpha^{eq}(\boldsymbol{x},t)}{\tau} \tag{8}$$

where $n_\alpha^{eq}(\boldsymbol{x},t)$ is called the equilibrium distribution function and τ is a relaxation time for collisions controlling the rate of approach to equilibrium. The form of the equilibrium distribution function depends on the particular lattice model chosen. The three-dimensional, "d3q15" model (12) which resides on a cubic lattice is used here (d3 indicates the model is three-dimensional, q15 refers to the number of components in the velocity space). The directions of the lattice velocities are shown in Figure 1. For this model, the equilibrium distribution function is given by

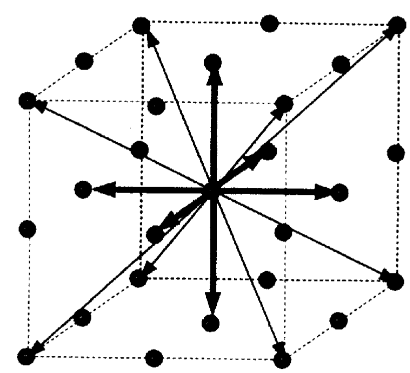

Figure 1: Base geometry and velocity vectors for the 3-D, 15-speed lattice Boltzmann model.

$$n_\alpha^{eq} = \frac{\rho}{9}\left(1 + 3\frac{(\boldsymbol{v}_\alpha \cdot \boldsymbol{u}^{eq})}{c} + \frac{9}{2}\frac{(\boldsymbol{v}_\alpha \cdot \boldsymbol{u}^{eq})^2}{c^2} - \frac{3}{2}\frac{(\boldsymbol{u}^{eq} \cdot \boldsymbol{u}^{eq})}{c^2} \right),\ \alpha=1,6 \tag{9}$$

$$n_\alpha^{eq} = \frac{\rho}{72}\left(1 + 3\frac{(\boldsymbol{v}_\alpha \cdot \boldsymbol{u}^{eq})}{c} + \frac{9}{2}\frac{(\boldsymbol{v}_\alpha \cdot \boldsymbol{u}^{eq})^2}{c^2} - \frac{3}{2}\frac{(\boldsymbol{u}^{eq} \cdot \boldsymbol{u}^{eq})}{c^2} \right),\ \alpha=7,14 \tag{10}$$

$$n_{15} = \frac{2}{9}\rho\left(1 - \frac{3}{2}\frac{(\boldsymbol{u}^{eq}\cdot\boldsymbol{u}^{eq})}{c^2}\right) \tag{11}$$

where

$$\boldsymbol{u}^{eq} = \boldsymbol{u} + \frac{\tau\boldsymbol{F}}{\rho} \tag{12}$$

and $\boldsymbol{v}_\alpha = c\boldsymbol{e}_\alpha$, $\boldsymbol{e}_\alpha$ are the unit vectors compromising the lattice directions in the discrete velocity space, c is the lattice velocity and $\boldsymbol{F}$ is a body force. To recover the physics associated with the Brinkman equation, the body force

$$\boldsymbol{F} = -s(\boldsymbol{x})\rho\boldsymbol{K}^{-1}\cdot\boldsymbol{u} \tag{13}$$

is introduced, where $s(\boldsymbol{x})$ is a characteristic function equal to 1 in porous media, and 0 in open regions. The approach has been validated in previous work (5).

Permeability for different flow directions was computed by imposing a constant pressure along opposite faces of the lattice in the desired direction and integrating the system of equations above to steady-state. Estimates for the intra-tow permeability values were obtained from the formulas given in (3). The steady-state velocity field at the inlet was integrated over the surface, A, to obtain the flow rate, Q, and this was used in the formula

$$K_{eff} = \frac{\mu QL}{A\Delta P} \tag{14}$$

to obtain the effective permeability, K_{eff}, for the desired direction.

EXPERIMENTAL

Composite Preparation

The epoxy resin system consisted of a diglycidyl ether of bisphenol A (DGEBA) monomer (Tactix123 , Dow Chemical Company, Midland, MI) and two amines[1]. Aromatic methylene dianiline (MDA) and aliphatic poly(propylene glycol)bis(2-aminopropyl ether) (JeffamineD400) (M_n~400) were purchased and used as received from Aldrich (Minneapolis, MN). The oxirane/ amine stoichiometry was 2 mol oxirane/1 mol amine. The amine

[1] Identification of a commercial product is made only to facilitate experimental reproducibility and to adequately describe experimental procedure. In no case does it imply endorsement by NIST or imply that it is necessarily the best product for the experimental procedure.

composition consisted of 0.07 mol MDA and 0.93 mol D400. The refractive index of the post-cured resin and of the fibers is 1.552$\pm$0.004 and 1.554$\pm$0.004, respectively, as measured by white light and index matching fluids. The refractive index of the epoxy composite is calculated by the rule of mixtures for the resin and the fiber volumes: V_{resin}=0.56, V_{fiber}=0.44, $(n_{resin})(V_{resin}) + (n_{fiber})(V_{fiber}) = n_{composite} = 1.55$. Details of the mixing and RTM are provided elsewhere (11).

OCT Instrumentation

The imaging system used in this study is shown schematically in Figure 2. OCT is based upon low-coherence optical ranging techniques where the optical distance to individual sites within the sample is determined by the difference in time, relative to a reference light beam, for an incident light beam to penetrate and backscatter within the sample. This temporal delay is probed using a fiber optic interferometer and a broadband laser light source. The fiber optic interferometer consists of a single-mode optical fiber coupled with a 50/50 fiber optic splitter that illuminates both the sample and a linearly translating reference mirror. Light reflected from the reference mirror recombines with light back-scattered and reflected from the sample at the 50/50 splitter to create a temporal interference pattern which is measured with a photodiode detector. The resulting interference patterns are present only when the optical path difference of the reference arm matches that of the sample arm to within the coherence length of the source. The axial, or y, spatial resolution that can be obtained with OCT is determined by the coherence length, or inverse spectral width, of the source and is typically 10-20 µm. The transverse, or x, spatial resolution of OCT is determined by the focal spot size on the sample which is typically 10-30 µm. Three-dimensional images of the sample are obtained by rastering the sample in x between successive OCT measurements along the z-axis. Further details of the system are found in reference (11).

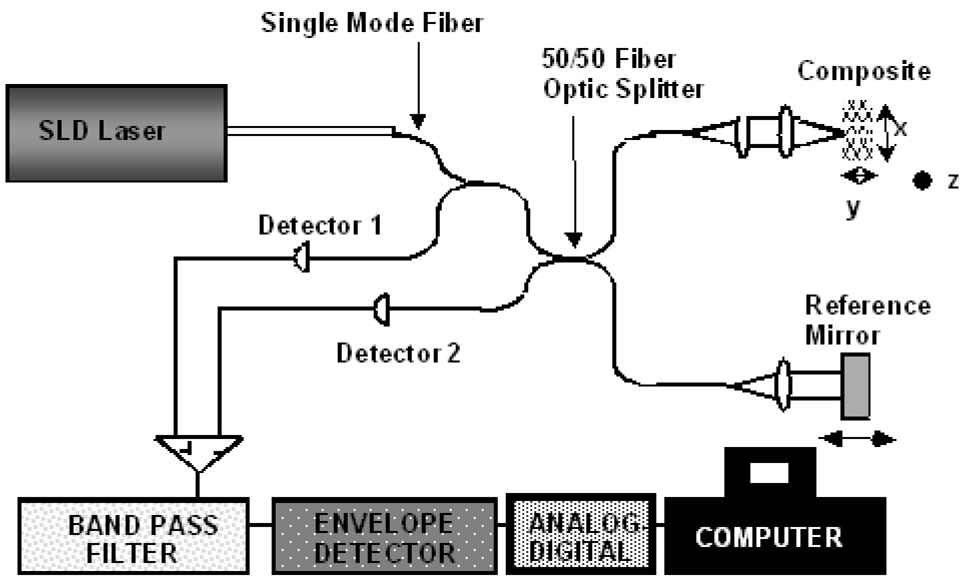

Figure 2: Schematic representation of the solid state laser and OCT system layout.

Image Processing

An automated image processing program was written using MATLAB 5.1 with the Image

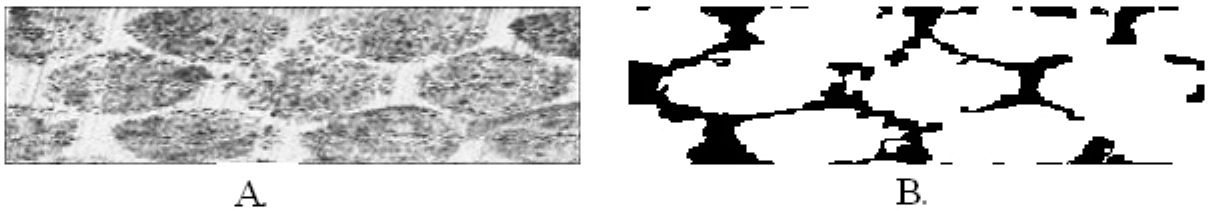

Figure 3: Original grayscale OCT image of the epoxy/ unidirectional E-glass composite. B. Binary OCT image after automated image processing.

Processing Toolbox to convert the raw gray scale OCT images to binary images of glass fiber and epoxy. An example is shown in Figure 3. The raw image is first rotated and cropped to eliminate sample tilt and edge effects, yielding an image such as in Figure 3a, where the darker ellipses correspond to the three cross-sectional layers of fiber tows while the lighter regions are due to the epoxy. To increase the contrast between the darker tows and the lighter epoxy regions, a variance image is created that replaces the intensity value of a 2x2 cluster of pixels with the standard deviation of that cluster. In the next two steps, spurious light pixels within the tow regions and vertical lines corresponding to detector saturation are eliminated. Using the automated program, the boundary of the tows are determined and a binary image (Figure 3b) is formed. An additional operation may be performed to smooth the rough boundaries of the tows. The resulting binary image is then used as input for the permeability modeling.

RESULTS AND DISCUSSION

Results from various permeability calculations are shown in Table 1. The value for the experimental permeability is a result from one axial flow experiment, and the error associated with it is taken from previous work with this reinforcement (13). Image sets within this table were processed using both the “Automated” procedure described above, and a “Manual” method. In the “Manual” method, the tow outlines were drawn by sight and filled in to obtain the binary image. In general, all the computationally predicted values are lower than the experimental value. The computational values that come closest to the experimental value are for samples Data 1 & 2, which were processed manually. However, sample Data 1 only utilizes 5 images in the z-direction and thus is not as complete a representation of the media. A direct comparison of the automated and manual processing can be made by comparing Data 2 and 3, which originate from the same raw image set. The automatically processed images in Data 3 yield an axial permeability of 2.83×10^{-4} mm^2 which is much lower than for Data 2. This result is somewhat surprising because the Brinkman fraction for Data 3 is slightly lower than for Data 2, which in general, should result in a higher permeability. From these results and from analysis of the fluid velocity data, we conclude that the roughness of the border between the tows and the resin has a large influence on the magnitude of the flow. The roughness results from noise in the original OCT images that the automated image processing routine is not able to eliminate. The influence of the roughness propagates to the middle of the channels between the tows where fluid velocity should be at a maximum. Sets Data 4 and Data 5 show that smoothing of the boundaries can be used to get closer agreement with the experimental values, but the smoothing results in some loss of Brinkman fraction.

Sample Name	Imaging Method	Image Set	Axial Permeability x 10^{-4} (mm^2)	Brinkman Fraction
Experiment	-	-	5.3 ± 1.1	0.770
Data 1	Manual	87-91	4.45	0.767
Data 2	Manual	75-95	3.81	0.788 ± 0.021
Data 3	Automated No Smoothing	75-95	2.83	0.768 ± 0.021
Data 4	Automated Smoothing	75-95	3.18	0.750 ± 0.027
Data 5	Automated Smoothing	4-24	5.09	0.727 ± 0.014
Data 6	Manual Roughened	75-95	2.73	0.795 ± 0.021
Data 7	Manual Dilated	75-95	2.99	0.837 ± 0.020

Table 1: Comparison of experimental and calculated permeabilities for different image processing methods.

This conclusion is further supported by results from samples Data 6 & 7. The images in these samples were derived from Data 2. In Data 6 the tow boundaries were roughened while keeping the same nominal Brinkman fraction; this artificial roughening lowers the permeability substantially. In Data 7, the tows were dilated to increase the Brinkman fraction but not the tow roughness. Significantly, even though the Brinkman fraction is roughly 4% higher in Data 7 than for Data 6, the permeability for Data 7 is higher. This comparison lends additional support to the idea that the noise induced tow roughness has a substantial impact on the predicted permeability, and highlights the importance of processing the images as close to the actual structure as possible.

Another significant result we have found is that the OCT / LB approach captures the effect of crossing threads on the permeability. In a previous paper (14) it was found that a 2-D calculation of the permeability for the Knytex material used here, which did not account for the crossing threads present in the material, yielded a permeability prediction roughly 6 times higher than the experimental value. A discrepancy which is quite unacceptable. The fact that the values computed here are on the same order of magnitude as the experimental value indicates that 3-D effect of the crossing threads is most likely being correctly captured.

SUMMARY

The microstructure of a glass reinforced composite was accurately and rapidly obtained using optical coherence tomography. OCT images were processed and input into a microscale flow model for permeability prediction. The axial permeability values, while not within 20% error, were considered reasonably good. The results highlighted the importance of boundary roughness generated during image processing.

ACKNOWLEDGEMENTS

This work was supported in part by a grant from the US Department of Commerce, contract 70NANB6H0092. We gratefully acknowledge technical contributions of Drs. Juergen Herrmann, Wolfgang Drexler, and Rohit Prasankumar. Michael A.A. Spaid helped develop the lattice Boltzmann code.

REFERENCES

1. Parnas, R. and Salem, A., Polymer Composites, 14(5), p. 383, (1993).
2. Friedman, H., Johnson, R., Miller, B., Salem, D., and Parnas, R., Polymer Composites, 18(5), p. 663, (1997).
3. Ranganathan, S., Wise, G., Phelan Jr., F., Parnas, R., and Advani, S. "Advanced Composites X: Proceedings of the 10th Annual ASM/ESD Advanced Composites Conference and Exposition (ACCE94)", ASM International, p. 309, (1994).
4. Phelan Jr., F. and Wise, G., Composites: Part A, 27A(1), p. 25, (1996).
5. Spaid, M. and Phelan Jr., F., Phys. Fluids, 9(9), p. 2468, (1997).
6. Spaid, M. and Phelan Jr., F., Composites: Part A, 29, p. 749, (1998).
7. Ranganathan, S., Easterling, R., Advani, S., and Phelan Jr., F., Polymers & Polymer Composites, 6(2), p. 63, (1998).
8. Huang, D., Swanson, E., Lin, C., Schuman, J., Stinson, W., Chang, W., Hee, M., Flotte, T., Gregory, K., Puliafito, C., and Fujimoto, J.G., Science, 254, p. 1178, (1991).
9. Fujimoto, J., Brezinski, M., Tearney, G. Boppart, S., Bouma, B., Hee, M. , Southern, J. and Swanson, E., Nature Medicine, 1, p. 970, (1995).
10. Bashkansky, M., Duncan, M., Kahn, M., Lewis, D., Reintjes, J., Opt. Lett., 22, 61(1997).
11. Dunkers, J., Parnas, R., Zimba, C., Peterson, R., Flynn, K., Fujimoto, J., and Bouma, B., Composites, Part A, 30, p. 139, (1999).
12. Hou, S., "Lattice Boltmann Method for Incompressible, Viscous Flow", Ph.D. Dissertation, Department of Mechanical Engineering, Kansas State University, Manhattan, Kansas, (1995).
13. Parnas, R., Flynn, K. and Dal-Favero, M., Polymer Composites, 18(5), p. 623, (1997).
14. Phelan Jr., F.R., Leung, Y., and Parnas, R.S., J. Therm. Comp. Mat., 7, p. 208, (1994).

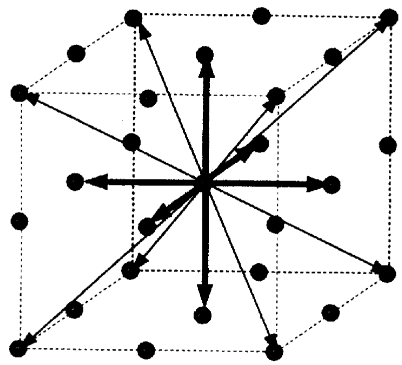

Figure 4: Base geometry and velocity vectors for the 3-D, 15-speed lattice Boltzmann model.

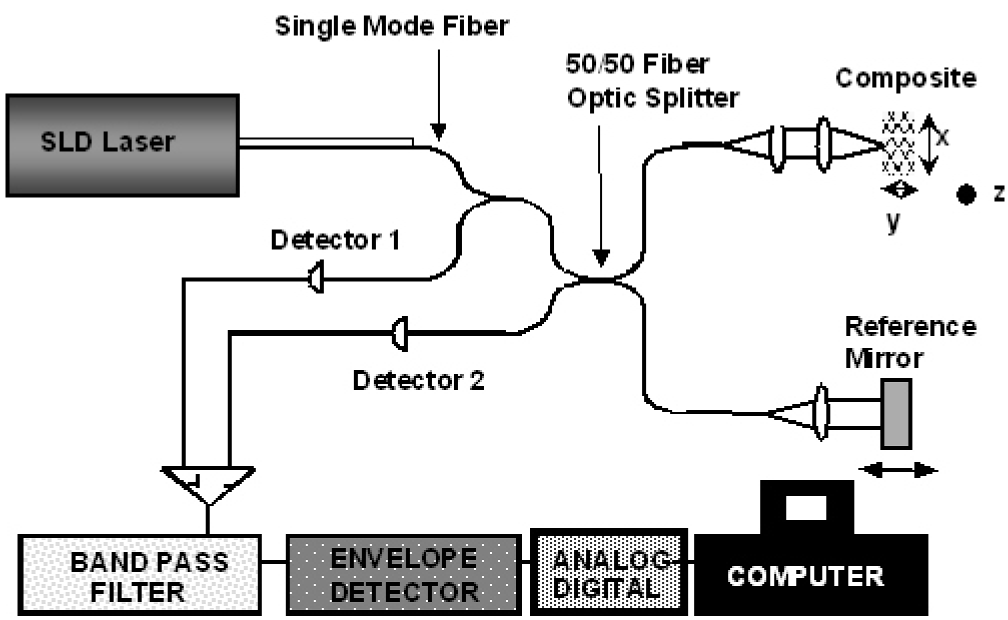

Figure 5: Schematic representation of the solid state laser and OCT system layout.

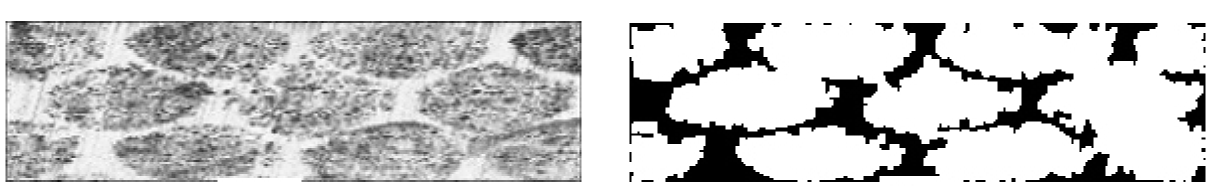

A. B.

Figure 6: A. Original grayscale OCT image of the epoxy/ unidirectional E-glass composite. B. Binary OCT image after automated image processing.

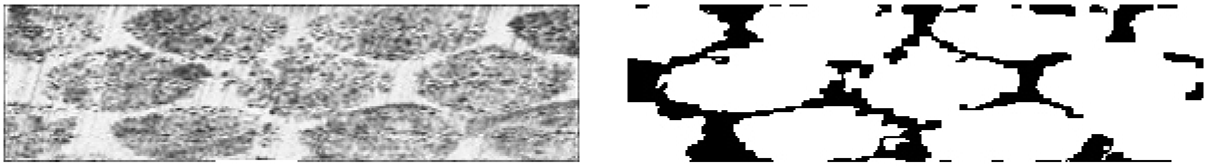

A. B.

Figure 7: Original grayscale OCT image of the epoxy/ unidirectional E-glass composite. B. Binary OCT image after automated image processing.